

An efficient direct band-gap transition in germanium by three-dimensional strain

S. Mellaerts¹, V. Afanasiev¹, J.W. Seo², M. Houssa^{1,3} and J.-P. Locquet¹

¹*Department of Physics and Astronomy, KU Leuven, Celestijnenlaan 200D, 3001 Leuven, Belgium,* ²*Department of Materials Engineering, KU Leuven, Kasteelpark Arenberg 44, 3001 Leuven, Belgium,* ³*Imec, Kapeldreef 75, 3001 Leuven, Belgium**

Complementary to the development of highly three-dimensional (3D) integrated circuits in the continuation of Moore's law, there has been a growing interest in new 3D deformation strategies to improve device performance. To continue this search for new 3D deformation techniques, it is essential to explore beforehand - using computational predictive methods - which strain tensor leads to the desired properties. In this work, we study germanium (Ge) under an isotropic 3D strain on the basis of first-principle methods. The transport and optical properties are studied by a fully *ab initio* Boltzmann transport equation and many-body Bethe-Salpeter equation (BSE) approach, respectively. Our findings show that a direct band gap in Ge could be realized with only 0.34% triaxial tensile strain (negative pressure) and without the challenges associated with Sn doping. At the same time a significant increase in refractive index and carrier mobility - particularly for electrons - is observed. These results demonstrate that there is a huge potential in exploring the 3D deformation space for semiconductors - and potentially many other materials - in order to optimize their properties.

I. INTRODUCTION

The advances in nanotechnology over the past decade have led to the continuation of Moore's law in the third dimension. As two-dimensional (2D) scaling of transistors is reaching its limit on various levels, there has been a development of 3D integration techniques which involves the vertical stacking and connecting of multiple functional materials and devices [1, 2]. This has led to an industry paradigm shift to explore the various benefits such an approach offers, including small form factor, multifunctionality as well as increased performance and yield.

This development also opens up a rich avenue for the exploration of epitaxially strained 3D materials. Epitaxial strain engineering is widely adopted in tuning and enhancing the functional properties of various materials including semiconductors [3–5] and oxide thin films [6–8]. However, in most cases, epitaxy involves the introduction of an in-plane strain by a lattice mismatch with the substrate, whereas the out-of-plane component is free to relax in order to sustain the induced stress in a nearly volume conserving manner. Furthermore, the lateral strain in thin films is limited by a critical thickness, above which the strain will slowly relax through the gradual introduction of misfit dislocations. A very recent approach promises to fundamentally alter this traditional picture. Through the engineering of vertically aligned nanocomposite (VAN) thin films it becomes possible to maintain the strain to much higher thickness by coupling to the vertical interfaces [9–11]. Once an epitaxial coupling to vertical interfaces can be realized, 3D tensile strain becomes envisionable.

In similar deviations from conventional epitaxy, there have been several attempts to access crystal phases deviating from their equilibrium crystal symmetry by the use of transfer methods. One example is the prediction and experimental realization of hexagonal Si, Ge and $\text{Si}_{1-x}\text{Ge}_x$ nanowires through crystal transfer methods in which a wurtzite gallium phosphide (GaP) nanowire core is used as template [12–15]. Furthermore, it was shown that hex- $\text{Si}_{1-x}\text{Ge}_x$ nanowires can have a direct band gap offering great opportunities for group III-V semiconductor opto-electronic devices.

In light of these new 3D material deformation strategies, we explore here the properties of 3D isotropically strained Ge. It has been shown recently that GeSn alloys grown on Si can also exhibit a direct band gap - depending on the amount of Sn doping - which is investigated in the context of both laser [16–20] and electronic applications [21–23]. On the other hand, a direct band gap has already been observed in $\langle 111 \rangle$ uniaxial and (001) biaxial tensile strained Ge at values $\sim 4\%$ ($E_g = 0.40$ eV) and $\sim 2\%$ ($E_g = 0.39$ eV), respectively [5, 24, 25]. Note that in such deformations, the cubic symmetry is lost which is detrimental for the valley degeneracies. In this work we demonstrate using an *ab initio* study that a symmetry conserving tensile strain above 0.34% in all three directions would be sufficient to induce a much larger direct band gap (716 meV) and circumventing the need for Sn doping in Ge.

II. COMPUTATIONAL METHODS

All calculations were performed within density functional theory (DFT) as implemented in the Vienna *ab initio* simulation package (VASP) [26]. The interactions between electrons and ions were described by the pro-

* simon.mellaerts@kuleuven.be

jector augmented wave (PAW) potentials [27], and the electronic wave functions were expanded with a cutoff energy of 500 eV. To study the various strained configurations, the choice of the exchange-correlation functional for the lattice and electronic band structure was optimized with respect to respectively the experimental lattice constant and energy gap of the unstrained configuration. For the ionic relaxation, phonon and elastic calculations the local density approximation (LDA) implemented by Ceperley-Alder was adopted [28]. For the structural relaxation, a force convergence criterion of 0.005 eV/Å was used with the Brillouin zone (BZ) sampled by a $12 \times 12 \times 12$ Γ -centered k -scheme. Phonon dispersions were calculated self-consistently on the basis of density functional perturbation theory (DFPT) and with the use of the PHONOPY package [29], while the stiffness matrix was calculated by a finite difference method as implemented in VASP.

For the electronic calculations, the improved hybrid functional for solids HSEsol [30] was chosen as it gave the best experimental agreement for the energy gap. The BZ was sampled by a $16 \times 16 \times 16$ Γ -centered k -scheme with energy convergence criterion of 10^{-6} eV.

To accurately describe the optical properties a fully self-consistent many-body approach was adopted [31]. As a starting point, the HSEsol calculated wave functions were used as input for the self-consistent Green's function (GW) method. Subsequently, these Green's functions are used to solve the Bethe-Salpeter equations (BSE) [32, 33], which take into account the excitonic effects. Due to the large computational expense of the BSE spectrum a less dense $8 \times 8 \times 8$ Γ -centered k -scheme is adopted.

An estimate of the transport properties was obtained by the use of the AMSET package. This approach completely relies on first-principle input parameters where the scattering rates are calculated by the Boltzmann transport equation (BTE) within the momentum relaxation time approximation (MRTA). To account for the band shifts and band warping the (anisotropic) deformation potentials were calculated via AMSET, resulting in relatively accurate mobility calculations at low computational expense [34].

III. RESULTS AND DISCUSSION

A. Structural and elastic properties

The structurally optimized face-centered cubic (fcc) unit cell with space group $Fd\bar{3}m$ (no. 227) is shown in Fig. 1. The lattice constant equals 5.65 Å, which is in agreement with the experimental value. An isotropic 3D strain ε , defined as $\varepsilon = (a - a_0)/a_0$, was applied along all three cubic lattice vectors within a range of -5% to $+5\%$ and stepsize 1%. Positive strain corresponds to a tensile expansion. For each strained configuration all atomic degrees were optimized. It was found that the space group is preserved and the Ge-Ge bond length changes linearly

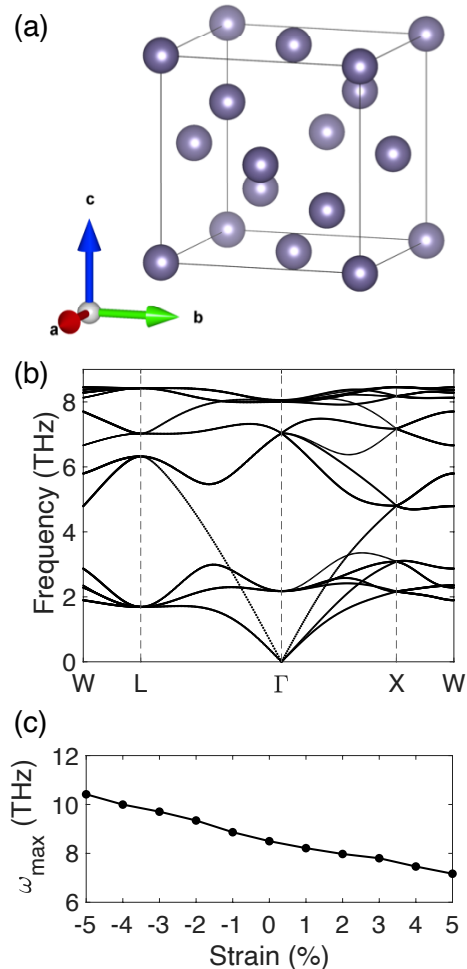


Figure 1. Lattice structure of germanium and its dynamical properties. (a) Conventional fcc unit cell. (b) Calculated phonon dispersion and (c) maximum phonon frequency as a function of 3D strain.

by the application of the isotropic strain.

By symmetry, the 6×6 stiffness matrix only consists of three independent stiffness constants C_{11} , C_{12} and C_{66} . From the finite difference method, the stiffness constants were calculated, from which the respective elastic parameters were derived: the bulk modulus (B), shear modulus (G), and Young's modulus (Y_s). These derived elastic parameters, which are summarized in Table I, are within 7% of the experimental parameters.

The dynamical properties of the equilibrium and strained configurations were determined by calculating the phonon dispersion. Our main quantity of interest here, is the cutoff phonon frequency ω_{max} which gives the upper bound for electron-phonon coupling interactions. It is shown in Fig. 1c that this cutoff frequency shows a linear dependence on hydrostatic pressure, where it decreases under 3D tensile strain. A similar trend has been observed in Si [35].

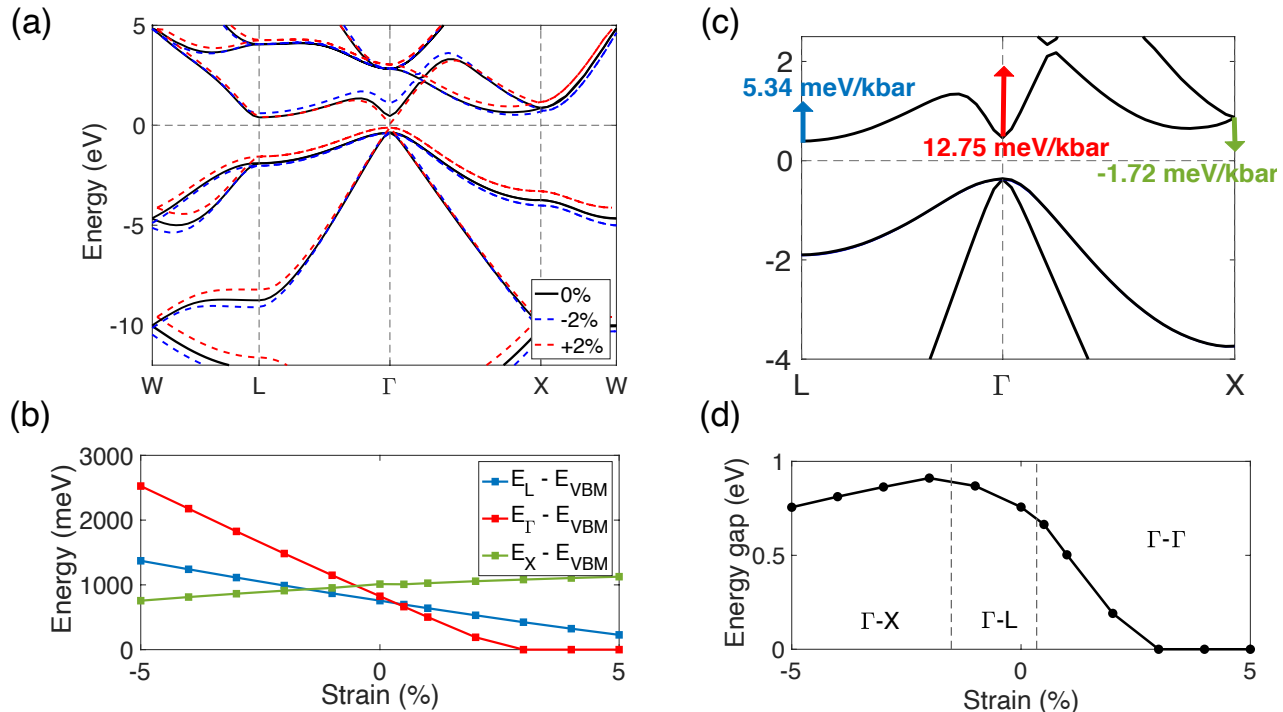


Figure 2. Electronic structure as a function of 3D strain. (a) The band structure as a function of strain and (b) the strain dependences of the band edges with respect to the VBM at Γ and (c) the derived pressure dependence of these band edges at the three BZ points [L, Γ , X]. (d) The evolution of the band gap as it evolves between 3 different CBM points in the BZ .

Table I. The DFT calculated stiffness constants and the derived elastic parameters compared to the experimental (Exp) values taken from [36].

	C_{11}	C_{12}	C_{66}	B	G	Y_s
DFT (kbar)	1197	475	600	716	361	927
Exp (kbar)	1260	480	670	740	390	995

B. Electronic band structure

To accurately describe the electronic band structure and to obtain experimental agreement with the energy gap, the improved hybrid functional for solids HSEsol was employed. The resulting band structure as a function of strain is shown in Fig. 2a. In the equilibrium situation the band structure of Ge has an indirect gap of 757 meV with its valence band maximum (VBM) located at the Γ point and conduction band minimum (CBM) at L. By evaluating the evolution of the band edges relative to VBM at Γ throughout the strain range (see Fig. 2b), the pressure dependence of the band edges was determined at three points in the BZ, as depicted in Fig. 2c. This agrees well with earlier predictions [37].

From the evolution of the band edges and the energy gap, shown in Fig. 2b-d, it is clear that the strong pressure dependence of the band edges allows two band gap transitions; from a compressive strain above 1.52% the

CBM changes from the L to X point, while a tensile strain of 0.34% induces a direct gap transition at Γ with an estimated gap value of 716 meV. On further increasing the tensile strain to 2.5% the direct gap at the Γ point will be closed and Ge becomes metallic, as derived from linear fitting of the Γ edge evolution in Fig. 2b. In contrast to the $\sim 4\%$ tensile $\langle 111 \rangle$ uniaxial ($E_g = 0.40$ eV) or $\sim 2\%$ tensile (001) biaxial strain ($E_g = 0.39$ eV) inducing a direct band gap [5], the 3D strain does not affect the degeneracy of the valleys, as symmetry is preserved. Moreover, from Fig. 2d, it is clear that the maximum direct band gap value that can be achieved is much larger compared to earlier approaches [12, 21, 38], while the 3D strain also allows the band gap to be tuned within this enlarged range of 0 – 716 meV.

Table II. The derived effective masses as a function of 3D strain.

Strain (%)	-5	-4	-3	-2	-1	0	+1	+2
m_e^*/m_0	0.846	0.821	0.835	0.851	0.129	0.110	0.035	0.032
m_{hh}^*/m_0	0.202	0.208	0.216	0.223	0.229	0.241	0.242	0.251
m_{lh}^*/m_0	0.091	0.086	0.083	0.077	0.072	0.066	0.061	0.060

Furthermore, the isotropic electron (m_e^*) and light/heavy hole (m_{lh}^*/m_{hh}^*) effective masses were derived from the curvature of the CBM and VBM valley, respectively, summarized in Table II. The induced

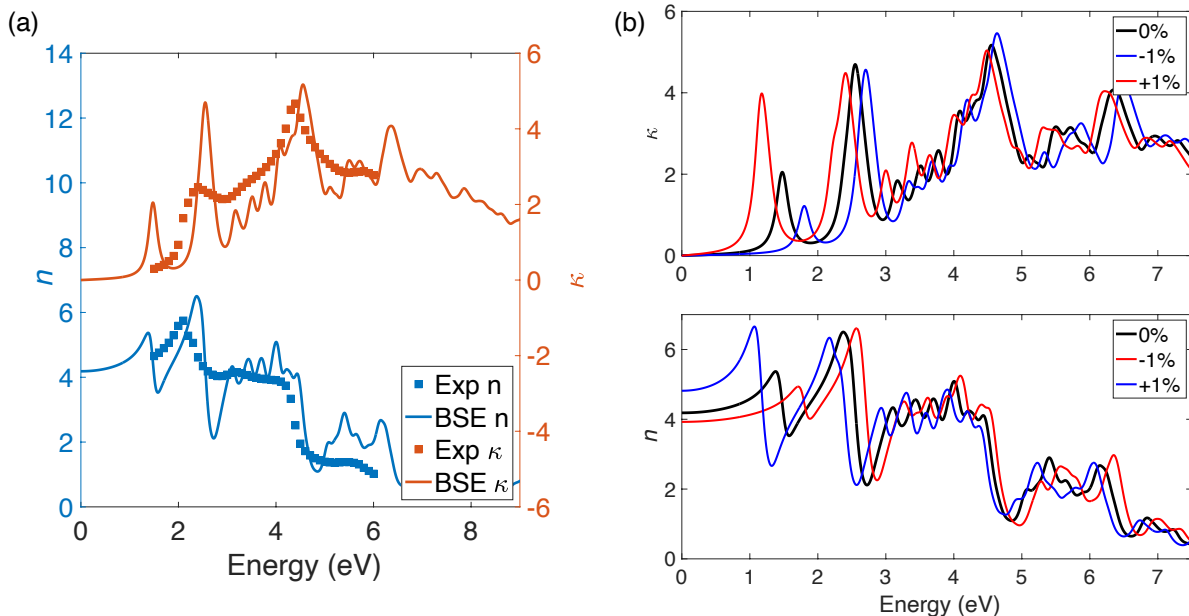


Figure 3. Optical properties as a function of 3D strain. (a) The GW-BSE calculated energy-dependent refractive index n and extinction coefficient κ compared to the experimental (Exp) data taken from [39]. (b) The strain dependence of κ and n .

hydrostatic pressure has relative little effect on the effective masses of the light and heavy holes in the Γ valley, nevertheless, the variation in position of the CBM valley is accompanied by drastic changes in the effective mass of the conduction electrons. Therefore, the realization of the direct gap at 0.34% tensile strain comes with the additional benefit of an extremely high decrease in the electron effective mass m_e^* at the CBM.

C. Optical properties

The establishment of a direct band gap whose value can be carefully tuned by the 3D strain opens the possibility of many optical applications. Therefore, the frequency-dependent dielectric function has been calculated by solving the BSE, taking into account excitonic effects. From the calculated complex dielectric function $\varepsilon = \varepsilon_1 + i\varepsilon_2$, the refractive index n and extinction coefficient κ were determined by

$$n = \frac{1}{\sqrt{2}} \left(\varepsilon_1 + (\varepsilon_1^2 + \varepsilon_2^2)^{1/2} \right)^{1/2}, \quad (1)$$

$$\kappa = \frac{1}{\sqrt{2}} \left(-\varepsilon_1 + (\varepsilon_1^2 + \varepsilon_2^2)^{1/2} \right)^{1/2}. \quad (2)$$

The resulting optical parameters are shown in Fig. 3a and reproduce well the main features of the experimental data [39]. Therefore, this self-consistent GW-BSE approach provides a good estimate of the optical properties, although it should be emphasized that the self-consistency in the GW calculation and the HSEsol wave

functions as input were crucial to obtain reliable results. Subsequently, the dielectric function and derived optical parameters for the different strained configurations were determined, whose trend in the tensile and compressive regime are depicted in Fig. 3b. Furthermore, an estimate of the static dielectric constant was obtained by the low-frequency asymptote of ε_1 . The static dielectric constants (ε_0) and corresponding refractive index (n) are summarized in Table III.

Table III. The derived static dielectric constant (ε_0) and refractive index (n) as a function of 3D strain.

Strain (%)	-5	-4	-3	-2	-1	0	+1	+2
ε_0	12.57	12.96	13.53	14.26	15.41	17.51	23.21	39.36
n	3.55	3.60	3.68	3.78	3.93	4.18	4.82	6.27

The transition to the direct band gap at 1% tensile strain causes a significant increase in the interband transition probability across the energy gap. This manifests itself in a drastic increase of the static dielectric permittivity and the redshift of the first peak in the extinction coefficient - proportional to the absorption coefficient - with a corresponding increase of factor 2. Since the symmetry and VBM degeneracy are preserved under 3D strain, the system becomes very similar to GaAs but with a much smaller energy gap. This offers great opportunities for infrared photodetectors [40, 41]. Alternatively, a small anisotropy in the 3D strain could be applied to induce LH and HH band splitting, where the LH band forms a low density of states (DOS) VBM, which facilitates population inversion, lowering the lasing

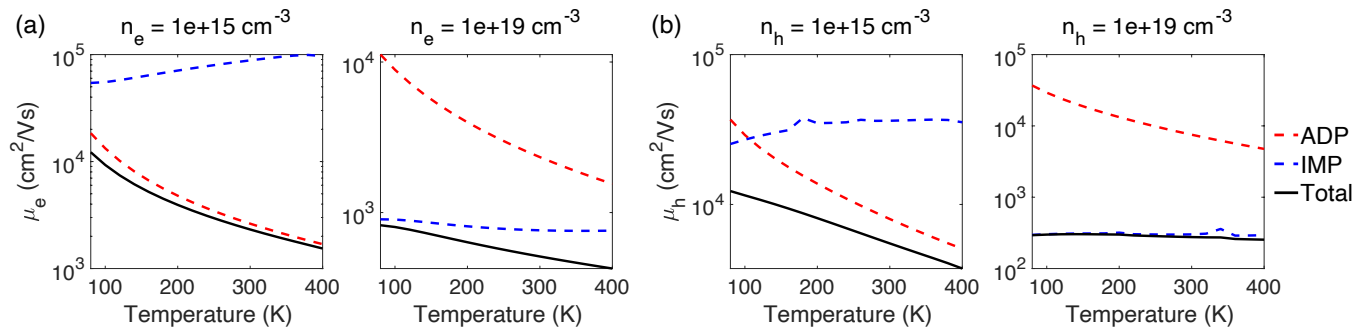


Figure 4. The (a) electron and (b) hole mobility as a function of doping concentration (n_e/n_h), and the respective contributions from acoustic deformation potential (ADP) scattering and impurity (IMP) scattering.

threshold [42]. In respect of achieving population inversion, the fraction of conduction electrons populating the Γ valley (N_Γ/N_{CB}) at an injection carrier density N_{inj} of 10^{19} cm^{-3} , which is a reasonable charge carrier density in the lasing regime [43], is calculated. By evaluation of the DOS with assuming a thermal broadening of 300 K, N_Γ/N_{CB} is found to be 4% and 9% for tensile strain of 0.5% ($E_\Gamma - E_L = 32 \text{ meV}$) and 1% ($E_\Gamma - E_L = 137 \text{ meV}$), respectively. These N_Γ/N_{CB} values are similar to what has been reported for the achieved $E_\Gamma - E_L$ in GeSn alloys, while a much larger N_Γ/N_{CB} fraction of 27% - twice the largest reported fraction [43] - can be achieved by a 2% triaxial tensile strain due to an extremely large valley difference $E_\Gamma - E_L = 340 \text{ meV}$.

D. Transport properties

The fully *ab initio* Boltzmann transport equation was solved within the MRTA while the scattering rates were evaluated by Fermi's Golden rule. As the fcc crystal structure of Ge is centrosymmetric the main scattering mechanisms consist of acoustic phonon scattering and impurity scattering, which are assumed to be elastic processes. The former scattering mechanism is implemented by an advanced acoustic deformation potential (ADP) scattering formalism that includes the scattering from both longitudinal and transverse modes in a single matrix element [34]. Therefore, a fully anisotropic deformation potential matrix was constructed by calculating the electronic structure under three inequivalent deformations. On the other hand, the quantum mechanical treatment of Brooks and Herring [44, 45] was adopted for approximating the impurity (IMP) scattering rate where the screening length was evaluated by the calculated DOS and static dielectric permittivity. Subsequently, the temperature-dependent electron/hole mobility (μ) was derived from the scattering rate and effective mass.

In this way, both temperature-dependent electron and

hole mobility were calculated for the unstrained case as a function of the doping concentration, depicted in Fig. 4. At low doping concentrations, the scattering rate is dominated by interactions with acoustic phonons, where carriers experience both intra- and intervalley scattering. At room temperature, the latter process becoming the main scattering mechanism due to the degenerate nature of the L valley. Therefore, uni- and biaxial strain have been successful in the enhancement of the electron mobility by lifting this degeneracy [38, 46]. While at higher doping concentrations, it is the impurity scattering that limits both electron and hole mobility.

Subsequently, the room-temperature electron and hole mobility were evaluated as a function of 3D strain and compared to the experimental data, shown in Fig. 5. At high doping concentrations, the simulated mobilities agree very well with the experimental data, whereas at lower doping concentrations the agreement is still within standard computational deviations. These deviations can be expected as the IMP scattering is much easier to calculate than ADP, since the latter strongly depends on small variations in the band energies.

In the compressive region, the electron mobility reduces slightly when the nature of the indirect gap changes with the CBM located at the X point. Conversely, the electron mobility increases significantly under 1–2% tensile strain, which can be mostly attributed to CBM located at the Γ with a reduced effective mass. This increased electron mobility is significant in the low doping regime where ADP scattering dominates, with a maximum enhancement of the electron mobility by a factor of 20–50 compared to pure Ge ($3900 \text{ cm}^2/\text{V}\cdot\text{s}$) at doping concentration 10^{15} cm^{-3} . The increase is less pronounced in the high doping regime where IMP scattering limits the mobility. In this latter situation, the enhancement is the result of the improved screening by an increased static dielectric permittivity ϵ_0 .

On the other hand, the induced hydrostatic pressure by 3D strain has a smaller effect on the hole mobility as the VBM degeneracy is preserved and the hole effective

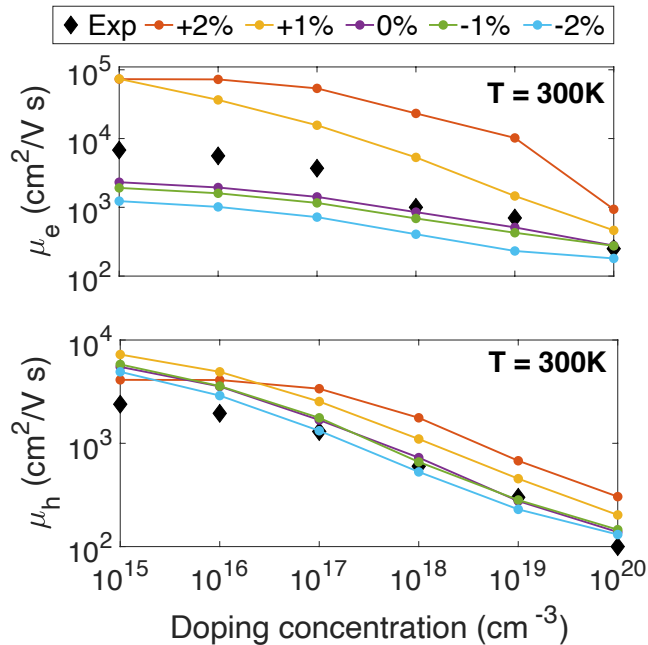


Figure 5. The room-temperature electron (top) and hole (bottom) mobility as a function of doping concentration for various strained configurations, compared to experimental data taken from [47, 48].

masses change only slightly. The hole mobility is nearly constant in the compressive region, while an increase of 50 – 100% is observed for 1 – 2% tensile strain in the high doping regime which can again be explained by the increased static dielectric permittivity ϵ_0 .

IV. DISCUSSION

To fully appreciate the potential of these results, a proper comparison to Sn alloying and uni- and biaxial strain should be made. Earlier computational work already pointed out that the perpendicular relaxation to the tensile strained direction is unfavorable to induce a direct gap transition. A direct gap transition without perpendicular relaxation could be achieved at 2.7% [111] uni- and 1% (001) biaxial strain, while due to perpendicular relaxation an additional 1% and 0.5% strain respectively is required [5]. From this perspective, it is not surprising to observe a direct gap transition at 0.34% tensile strain in all three spatial directions. In following, the advantages in the low and high band gap regime in electronic and optical applications are discussed.

Our first-principle calculations suggest that this 3D strain offers great opportunities for Ge high-mobility transistors with several advantages over current approaches. The enhancement in electron mobility by a factor of 20 – 50 compared to pure Ge at doping concentra-

tion 10^{15} cm^{-3} is quantitatively very similar to maximum mobilities achieved in highly uni- and biaxial strained Ge and GeSn alloys [22, 38]. This can be expected as they all rely on the inducement of a direct gap where the mobility is determined by the conduction electrons populating the Γ valley with a reduced effective mass. Nonetheless, we expect that the enhancement of the electron mobility should also be more substantial for 3D strain induced lower band gap states compared GeSn systems where an increasing Sn alloy disorder scattering becomes detrimental for the electrons populating the Γ valley [22].

In addition, our results suggest that these current approaches are inefficient in achieving a direct band gap as their maximum possible direct gap is relatively low. In contrast to 3D strain with a maximum direct gap value of 0.72 eV, a much lower value of 0.40 eV and 0.39 eV is found for uni- and biaxial strain respectively [5], and a similar value of 0.48 eV for GeSn alloys [21]. These lower band gap values impose strong constraints on the performance of high-mobility devices.

This also has implications for optical devices, where a much larger direct gap value range (0 – 716 meV) can be covered by the 3D strain within an experimental accessible strain range of $\sim 2.5\%$, achievable by the use of $\text{In}_x\text{Ga}_{1-x}\text{As}$ buffer layers [49]. This becomes particularly interesting in the search for group III-V semiconductor opto-electronic applications where lower band gap values are required to cover the complete infrared region (e.g. gas sensing at $5 \mu\text{m}/248 \text{ meV}$). Achieving these lower gap values in GeSn alloys would require very high Sn concentrations, which quickly becomes experimentally challenging due to frequent Sn precipitation [50]. Furthermore, random alloy fluctuations and band mixing lead to inhomogeneous broadening of the band edges and gain spectrum, resulting in the increase of the lasing threshold [37]. An other major concern is the relatively low DOS of the CBM which puts constraints on the density of electrons that can be excited to the Γ valley before saturation and spill over to the L valley. Achieving a direct gap nature at much higher gap value by 3D strain implies an increased $E_\Gamma - E_L$ and corresponding increase of the fraction of conduction electrons populating the Γ valley (N_Γ/N_{CB}) at the required band gap value for infrared lasing. The current GeSn lasers are operating with band gap values of 460 meV and $E_\Gamma - E_L < 70 \text{ meV}$ [20, 42], whereas by 3D strain of 1.1% the same direct gap could be achieved with an increased valley energy difference of 164 meV. These differences will increase further in the achievement of higher wavelength lasers, which again shows the advantages of efficiently inducing a direct band gap in Ge through 3D strain (negative pressure).

Although this remains experimentally unexplored for Ge, we suggest that the inducement of 3D strain might - besides using VAN's - also be achieved by the gradual introduction of strain through a thermal expansion mismatch with the substrate. In this way, the epitaxial deposition of Ge in a Si micrometer trench would

allow a tensile strain of 0.25% in all three directions [51, 52]. By interpolation of our data, this would result in a nearly direct band gap with only an energy difference of $E_L - E_\Gamma = 17$ meV. This is in contrast to 0.25% biaxially strained Ge on Si with $E_L - E_\Gamma = 115$ meV [52], which has been used as a lasing platform. However, in this situation a high n-doping concentration of $\sim 10^{19}$ cm $^{-3}$ is required to compensate for the indirect gap nature and to fill the L valley. Therefore, our proposed scheme could circumvent the need of this extremely high n-doping which is accompanied by large free carrier absorption loss and an increasing lasing threshold.

V. CONCLUSIONS

Our first-principle simulations predict that 3D strain offers a very interesting and efficient alternative route for the realization of a direct band gap in single crystalline Ge. This has several advantages including a precise control of the band gap value which allows coverage of the whole infrared emission region within the experimental feasible strain range of $\sim 2.5\%$, essential for optical implementations. In this context, 3D strain prevents vari-

ous disadvantages of the Sn alloying of Ge method where random alloy fluctuations limit the electron mobility at lower band gap values, and band mixing effects lead to inhomogeneous broadening of the band edges and gain spectrum, increasing the lasing threshold [37]. We hope these findings will stimulate the search for new 3D deformations techniques as an alternative to current approaches. As a future step, also anisotropic 3D strains should be considered since these will for instance enable to control the existence of the degeneracies in the respective valleys.

ACKNOWLEDGEMENTS

Part of this work was financially supported by the KU Leuven Research Funds, Project No. KAC24/18/056 and No. C14/17/080 as well as the Research Funds of the INTERREG-E-TEST Project (EMR113) and INTERREG-VL-NL-ETPATHFINDER Project (0559). Part of the computational resources and services used in this work were provided by the VSC (Flemish Supercomputer Center) funded by the Research Foundation Flanders (FWO) and the Flemish government.

-
- [1] Mukta G. Farooq and Subramanian S. Iyer. 3d integration review. *Science China Information Sciences*, 54(5):1012, 2011.
 - [2] A. W. Topol, D. C. L. Tulipe, L. Shi, D. J. Frank, K. Bernstein, S. E. Steen, A. Kumar, G. U. Singco, A. M. Young, K. W. Guarini, and M. Jeong. Three-dimensional integrated circuits. *IBM Journal of Research and Development*, 50(4.5):491–506, 2006.
 - [3] S. E. Thompson, Guangyu Sun, Youn Sung Choi, and T. Nishida. Uniaxial-process-induced strained-si: extending the cmos roadmap. *IEEE Transactions on Electron Devices*, 53(5):1010–1020, 2006.
 - [4] Y. Sun, S. E. Thompson, and T. Nishida. Physics of strain effects in semiconductors and metal-oxide-semiconductor field-effect transistors. *Journal of Applied Physics*, 101(10):104503, 2007.
 - [5] T. Inaoka, T. Furukawa, R. Toma, and S. Yanagisawa. Tensile-strain effect of inducing the indirect-to-direct band-gap transition and reducing the band-gap energy of ge. *Journal of Applied Physics*, 118(10):105704, 2015.
 - [6] J. P. Locquet, J. Perret, J. Fompeyrine, E. Mächler, J. W. Seo, and G. Van Tendeloo. Doubling the critical temperature of $\text{La}_{1.9}\text{Sr}_{0.1}\text{CuO}_4$ using epitaxial strain. *Nature*, 394(6692):453–456, 1998.
 - [7] L. Dillemans, R.R. Lieten, M. Menghini, T. Smets, J.W. Seo, and J.-P. Locquet. Correlation between strain and the metal–insulator transition in epitaxial V_2O_3 thin films grown by molecular beam epitaxy. *Thin Solid Films*, 520(14):4730 – 4733, 2012. Proceedings of the EMRS 2011 Spring Meeting Symposium D: Synthesis, Processing and Characterization of Nanoscale Multi Functional Oxide Films III.
 - [8] P. Homm, M. Menghini, J. W. Seo, S. Peters, and J. P. Locquet. Room temperature mott metal-insulator transition in V_2O_3 compounds induced via strain-engineering. *APL Materials*, 9(2):021116, 2021.
 - [9] X. Sun, J. Huang, J. Jian, M. Fan, H. Wang, Q. Li, J. L. Mac Manus-Driscoll, P. Lu, X. Zhang, and H. Wang. Three-dimensional strain engineering in epitaxial vertically aligned nanocomposite thin films with tunable magnetotransport properties. *Mater. Horiz.*, 5:536–544, 2018.
 - [10] J. L. MacManus-Driscoll, P. Zerrer, H. Wang, H. Yang, J. Yoon, A. Fouchet, R. Yu, M. G. Blamire, and Q. Jia. Strain control and spontaneous phase ordering in vertical nanocomposite heteroepitaxial thin films. *Nature Materials*, 7(4):314–320, 2008.
 - [11] X. Sun, Q. Li, J. Huang, J. Jian, P. Lu, X. Zhang, J. L. MacManus-Driscoll, and H. Wang. Strain and property tuning of the 3D framed epitaxial nanocomposite thin films via interlayer thickness variation. *Journal of Applied Physics*, 125(8):082530, 2019.
 - [12] X. Cartoixà, M. Palummo, H. I. T. Hauge, E. P. A. M. Bakkers, and R. Rurali. Optical emission in hexagonal sige nanowires. *Nano Letters*, 17(8):4753–4758, 08 2017.
 - [13] H. I. T. Hauge, M. A. Verheijen, S. Conesa-Boj, T. Etzelstorfer, M. Watzinger, D. Kriegner, I. Zardo, C. Fasolato, F. Capitani, P. Postorino, S. Kölling, A. Li, S. Assali, J. Stangl, and E. P. A. M. Bakkers. Hexagonal silicon realized. *Nano Letters*, 15(9):5855–5860, 09 2015.
 - [14] H. I. T. Hauge, S. Conesa-Boj, M. A. Verheijen, S. Koelling, and E. P. A. M. Bakkers. Single-crystalline hexagonal silicon–germanium. *Nano Letters*, 17(1):85–90, 01 2017.
 - [15] E. M. T. Fadaly, A. Dijkstra, J. R. Suckert, D. Ziss, M. A. J. van Tilburg, C. Mao, Y. Ren, V. T. van

- Lange, K. Korzun, S. Kölling, M. A. Verheijen, D. Busse, C. Rödl, J. Furthmüller, F. Bechstedt, J. Stangl, J. J. Finley, S. Botti, J. E. M. Haverkort, and E. P. A. M. Bakkers. Direct-bandgap emission from hexagonal ge and sige alloys. *Nature*, 580(7802):205–209, 2020.
- [16] S. Gupta, B. Magyari-Köpe, Y. Nishi, and K. C. Saraswat. Achieving direct band gap in germanium through integration of sn alloying and external strain. *Journal of Applied Physics*, 113(7):073707, 2013.
- [17] C. Eckhardt, K. Hummer, and G. Kresse. Indirect-to-direct gap transition in strained and unstrained $\text{Sn}_x\text{Ge}_{1-x}$ alloys. *Phys. Rev. B*, 89:165201, Apr 2014.
- [18] R. Chen, H. Lin, Y. Huo, C. Hitzman, T. I. Kamins, and J. S. Harris. Increased photoluminescence of strain-reduced, high-Sn composition $\text{Ge}_{1-x}\text{Sn}_x$ alloys grown by molecular beam epitaxy. *Applied Physics Letters*, 99(18):181125, 2011.
- [19] S. Al-Kabi, S. A. Ghetmiri, J. Margetis, T. Pham, Y. Zhou, W. Dou, B. Collier, R. Quinde, W. Du, A. Mosleh, J. Liu, G. Sun, R. A. Soref, J. Tolle, B. Li, M. Mortazavi, H. A. Naseem, and S.-Q. Yu. An optically pumped 2.5 μm GeSn laser on Si operating at 110 k. *Applied Physics Letters*, 109(17):171105, 2021/01/24 2016.
- [20] S. Wirths, R. Geiger, N. von den Driesch, G. Mussler, T. Stoica, S. Mantl, Z. Ikonc, M. Luysberg, S. Chiussi, J. M. Hartmann, H. Sigg, J. Faist, D. Buca, and D. Grützmacher. Lasing in direct-bandgap GeSn alloy grown on Si. *Nature Photonics*, 9(2):88–92, 2015.
- [21] K. Lu Low, Y. Yang, G. Han, W. Fan, and Y.-C. Yeo. Electronic band structure and effective mass parameters of $\text{Ge}_{1-x}\text{Sn}_x$ alloys. *Journal of Applied Physics*, 112(10):103715, 2012.
- [22] B. Mukhopadhyay, G. Sen, R. Basu, S. Mukhopadhyay, and P. K. Basu. Prediction of large enhancement of electron mobility in direct gap $\text{Ge}_{1-x}\text{Sn}_x$ alloy. *physica status solidi (b)*, 254(11):1700244, 2017.
- [23] Noriyuki Uchida, Junichi Hattori, Ruben R. Lieten, Yuji Ohishi, Ryohei Takase, Manabu Ishimaru, Koichi Fukuda, Tatsuro Maeda, and Jean-Pierre Locquet. Carrier and heat transport properties of poly-crystalline gesn films for thin-film transistor applications. *Journal of Applied Physics*, 126(14):145105, 2019.
- [24] F. Zhang, V. H. Crespi, and P. Zhang. Prediction that uniaxial tension along $\langle 111 \rangle$ produces a direct band gap in germanium. *Phys. Rev. Lett.*, 102:156401, Apr 2009.
- [25] Richard A. S. and Lionel F. Direct-gap Ge/GeSn/Si and GeSn/Ge/Si heterostructures. *Superlattices and Microstructures*, 14(2):189 – 193, 1993.
- [26] G. Kresse and J. Furthmüller. Efficient iterative schemes for ab initio total-energy calculations using a plane-wave basis set. *Phys. Rev. B*, 54:11169–11186, Oct 1996.
- [27] G. Kresse and D. Joubert. From ultrasoft pseudopotentials to the projector augmented-wave method. *Phys. Rev. B*, 59:1758–1775, Jan 1999.
- [28] D. M. Ceperley and B. J. Alder. Ground state of the electron gas by a stochastic method. *Phys. Rev. Lett.*, 45:566–569, Aug 1980.
- [29] A. Togo and I. Tanaka. First principles phonon calculations in materials science. *Scr. Mater.*, 108:1–5, Nov 2015.
- [30] L. Schimka, J. Harl, and G. Kresse. Improved hybrid functional for solids: The hsesol functional. *The Journal of Chemical Physics*, 134(2):024116, 2011.
- [31] T. Sander, E. Maggio, and G. Kresse. Beyond the tamm-dancoff approximation for extended systems using exact diagonalization. *Phys. Rev. B*, 92:045209, Jul 2015.
- [32] S. Albrecht, L. Reining, R. Del Sole, and G. Onida. Ab initio calculation of excitonic effects in the optical spectra of semiconductors. *Phys. Rev. Lett.*, 80:4510–4513, May 1998.
- [33] M. Rohlfing and S. G. Louie. Electron-hole excitations in semiconductors and insulators. *Phys. Rev. Lett.*, 81:2312–2315, Sep 1998.
- [34] A. M. Ganose, J. Park, A. Faghaninia, R. Woods-Robinson, K. A. Persson, and A. Jain. Efficient calculation of carrier scattering rates from first principles, 2020.
- [35] C. Kim and R. Ramprasad. Dielectric breakdown field of strained silicon under hydrostatic pressure. *Applied Physics Letters*, 111(11):112904, 2017.
- [36] P. N. Keating. Theory of the third-order elastic constants of diamond-like crystals. *Phys. Rev.*, 149:674–678, Sep 1966.
- [37] T. D. Eales, I. P. Marko, S. Schulz, E. O’Halloran, S. Ghetmiri, W. Du, Y. Zhou, S.-Q. Yu, J. Margetis, J. Tolle, E. P. O’Reilly, and S. J. Sweeney. $\text{Ge}_{1-x}\text{Sn}_x$ alloys: Consequences of band mixing effects for the evolution of the band gap Γ -character with Sn concentration. *Scientific Reports*, 9(1):14077, 2019.
- [38] F. Murphy-Armando and S. Fahy. Giant enhancement of n-type carrier mobility in highly strained germanium nanostructures. *Journal of Applied Physics*, 109(11):113703, 2011.
- [39] D. E. Aspnes and A. A. Studna. Dielectric functions and optical parameters of Si, Ge, GaP, GaAs, GaSb, InP, InAs, and InSb from 1.5 to 6.0 eV. *Phys. Rev. B*, 27:985–1009, Jan 1983.
- [40] Y. F. Lao, A. G. U. Perera, H. L. Wang, J. H. Zhao, Y. J. Jin, and D. H. Zhang. Optical characteristics of p-type GaAs-based semiconductors towards applications in photoemission infrared detectors. *Journal of Applied Physics*, 119(10):105304, 2016.
- [41] H. C. Liu, C. Y. Song, A. Shen, M. Gao, Z. R. Wasilewski, and M. Buchanan. Gaas/algaas quantum-well photodetector for visible and middle infrared dual-band detection. *Applied Physics Letters*, 77(16):2437–2439, 2000.
- [42] A. Elbaz, D. Buca, N. von den Driesch, K. Pantzas, G. Patriarche, N. Zerounian, E. Herth, X. Checoury, S. Sauvage, I. Sagnes, A. Foti, R. Ossikovski, J.-M. Hartmann, F. Boeuf, Z. Ikonc, P. Boucaud, D. Grützmacher, and M. El Kurdi. Ultra-low-threshold continuous-wave and pulsed lasing in tensile-strained gesn alloys. *Nature Photonics*, 14(6):375–382, 2020.
- [43] Denis Rainko, Zoran Ikonc, Anas Elbaz, Nils von den Driesch, Daniela Stange, Etienne Herth, Philippe Boucaud, Moustafa El Kurdi, Detlev Grützmacher, and Dan Buca. Impact of tensile strain on low sn content gesn lasing. *Scientific Reports*, 9(1):259, 2019.
- [44] H. Brooks. Scattering by ionized impurities in semiconductors. In *Physical Review*, volume 83, pages 879–879. AMERICAN PHYSICAL SOC ONE PHYSICS ELLIPSE, COLLEGE PK, MD 20740-3844 USA, 1951.
- [45] C. Herring and E. Vogt. Transport and deformation-potential theory for many-valley semiconductors with anisotropic scattering. *Phys. Rev.*, 101:944–961, Feb 1956.
- [46] S. Ran, T. S. Glen, B. Li, D. Shi, I. Choi, E. A. Fitzgerald, and S. T. Boles. The limits of electromechanical cou-

- pling in highly-tensile strained germanium. *Nano Letters*, 20(5):3492–3498, 2020. PMID: 32302152.
- [47] V. I. Fistul, M. I. Iglitsyn, and E. M. Omelyanovskii. Mobility of electrons in germanium strongly doped with arsenic. *Sov. Phys. Solid State*, 9(4):784–785, 1962.
- [48] O. A. Golikova, B. Y. Moizhez, and L. S. Stilbans. Hole mobility of germanium as a function of concentration and temperature. *Sov. Phys. Solid State*, 9(3):2259–2265, 1962.
- [49] Y. Huo, H. Lin, R. Chen, M. Makarova, Y. Rong, M. Li, T. I. Kamins, J. Vuckovic, and J. S. Harris. Strong enhancement of direct transition photoluminescence with highly tensile-strained ge grown by molecular beam epitaxy. *Applied Physics Letters*, 98(1):011111, 2011.
- [50] S. Zaima, O. Nakatsuka, N. Taoka, M. Kurosawa, W. Takeuchi, and M. Sakashita. Growth and applications of gesn-related group-iv semiconductor materials. *Science and Technology of Advanced Materials*, 16(4):043502, 2015. PMID: 27877818.
- [51] Jifeng Liu, Douglas D. Cannon, Kazumi Wada, Yasuhiko Ishikawa, David T. Danielson, Samerkhay Jongthammurak, Jurgen Michel, and Lionel C. Kimerling. Deformation potential constants of biaxially tensile stressed Ge epitaxial films on Si(100). *Phys. Rev. B*, 70:155309, Oct 2004.
- [52] Jifeng Liu, Xiaochen Sun, Dong Pan, Xiaoxin Wang, Lionel C. Kimerling, Thomas L. Koch, and Jurgen Michel. Tensile-strained, n-type Ge as a gain medium for monolithic laser integration on Si. *Opt. Express*, 15(18):11272–11277, Sep 2007.